CONSTITUTIVE AND NUMERICAL MODELLING FOR TIMBER-METAL CONNECTIONS UNDER LARGE DEFORMATIONS

Labuwatte Manathum Milindu Bandara Jayasekara

PhD Student, Department of Engineering, University of Cambridge, United Kingdom.

lmmbj2@cam.ac.uk

Robert M Foster

University Associate Professor, Department of Engineering, University of Cambridge, United Kingdom.

Corresponding Author: rmf41@cam.ac.uk

Abstract

Computational modelling of complex timber-metal connections undergoing large deformations is crucial for the design of safe and robust multi-storey timber structures. Accurate simulation through large deformations requires constitutive models that suitably capture the full post-elastic behaviour of materials. Post-elastic behaviour of timber is particularly challenging to model due to strong anisotropy and material non-linearity in the post-elastic regime. Efficient simulation of complex connections requires advanced numerical modelling techniques to expedite explicit solution in the finite element domain. In this study, a suitable constitutive model for ductile metal components through large deformations, including consideration of stress localisation and triaxiality post-necking, is described. Some existing constitutive models for timber are discussed, and new constitutive models capturing both ductile and brittle failure modes are presented. A new formulation of the Hoffmann yield criterion with isotropic hardening for explicit solution is presented, and new VUMAT user subroutines for explicit solution in ABAQUS for Hoffmann, Sandhaas, Gharib, Hill-Gharib and Hoffmann-Gharib models are developed and made available for the benefit of other researchers. A benchmarked numerical model incorporating advanced modelling techniques to improve computational efficiency without compromising accuracy is presented for a complex timber, aluminium and steel dowelled beam-column connection tested shear and moment dominated testing. The simulation results compare favourably with experimental results in the literature, demonstrate that the proposed constitutive models and numerical modelling techniques provide realistic predictions of behaviour, including failure mode, and thus have the potential to support the design of complex timber-metal connections through large deformations under quasi-static and dynamic loading.

Keywords: Timber-metal connections, Large deformation, Constitutive modelling, Continuum damage modelling, Explicit finite element analysis

1 Introduction

Computational modelling of complex timber-metal connection behaviour is vital for the design of reliable and efficient timber structures. The strongly anisotropic nature of timber, with differing stiffness, strength and failure mode in different material directions, present challenges for constitutive modelling [1]. The design of alternative load paths necessary to ensure robustness in the event of element removal requires accurate post-elastic modelling through large deformations [2]. The ongoing development of increasingly sophisticated timber connections – typically multi-material assemblages incorporating metals such as steel and aluminium, in addition to one or more timber or engineered timber materials – further increases the complexity and computational cost of detailed numerical models.

Modelling of timber connections is often simplified by considering: elastic-plastic behaviour without consideration of failure [3], [4]; simple dowel-type connectors [5], [6], [7]; one material or performance parameter of a connection [8], [9], [10], [11]; or predefined failure modes [12], [13]. Most prior studies employ numerical solution by backward Euler approximation. Use of the forward Euler approximation method for simulating complex, non-linear or dynamic behaviour of timber connections is limited and require further development [4], [14], [15].

Well-established numerical methods based on the Von Mises criterion exist to model the failure of metal components in bolted assemblies [16], [17]. Failure theories for timber under compression and tension exist for 1D, 2D and 3D simulations [18], [19]. Commonly used single-surface 3D elastic-plastic yield criteria such as Hill [20], Hoffman [21] and Tsai-Wu [22] can incorporate the anisotropic yielding of timber under compression but are unable to accommodate the brittle tensile failure of timber. The Hill criterion assumes that only deviatoric stresses contribute to yielding and applications in the literature suggest promising results [3], [4], [13], [23]. The Hoffman criterion is an extension of the Hill criterion that also considers hydrostatic stresses and differences in compressive and tensile strengths in each material direction. Some studies report better results using

the Hoffman criterion in comparison to the Hill criterion, while others indicate the opposite [24], [25], [26], [27], [28]. These conflicting results may be attributable to the contribution of hydrostatic stresses towards yielding varying for different timber specimens [29]. The use of the more general Tsai-Wu criterion is typically limited by the requirement for empirical stress interaction coefficients that are difficult to obtain experimentally.

Complex multi-surface failure theories [30], [31] and micro-mechanical modelling techniques [32] have been developed for timber but have found limited application due to the sophistication of the material laws, difficulties in implementation and numerical instability. A simpler multi-surface criterion is proposed by Hashin based on unidirectional fibre composites considering four failure modes [15], [33]. Sandhaas et al [34] propose a constitutive model combining a three-dimensional (3D) failure criterion, incorporating eight distinct failure modes based on maximum principal stress theory, with continuum damage mechanics. The Sandhaas model is relatively easy to implement and has shown promising results [14], [35] but may suffer from rapid artificial softening, producing spurious energies and inaccurate results [34]. Gharib et al [36] propose a modified version of the Sandhaas model including a well-defined softening response with residual stiffness, improving numerical stability [37]. Others have proposed using plastic yield criteria with continuum damage modelling to initiate brittle failure [38], [39]. However, these approaches include isotropic damage and are unable to consider differences in tensile and compressive strength. Eslami et al [29] and Wang et al [40] employ composite failure criteria, combining plastic yield criteria for compression with the Sandhaas maximum principal stress based criterion for brittle tensile failure, through backward-Euler approximations. However, due to the numerical procedures adopted, compression behaviour is primarily governed by the maximum principal stress-based criterion rather than plastic yield criterion. All these models have been applied mostly in simple dowel-type connections or simple beam-bending simulations using backward Euler methods, and their performance in modelling complex assemblages under various stress states is unknown.

This study presents constitutive models and numerical modelling for complex multi-material metal-timber connections through large deformations, as required for robust design of timber buildings. Section 2 explores suitable constitutive models for metals and timber, and proposes new timber failure criteria. These criteria and their implementation in the finite element (FE) method, combining the explicit solving capability of the commercially available ABAQUS FE software with new VUMAT user subroutines developed in this study are also explained. These subroutines are made available for the benefit of other researchers. Section 3 provides a benchmarked numerical example, applying the models developed in Section 2 to a complex multi-material steel, aluminium and Laminated Veneer Lumber (LVL) post-and-beam timber connection. Modelling considerations affecting accuracy and efficiency are discussed, and model performance under different loading configurations is assessed. The conclusions of the study are presented in Section 4.

2 Constitutive models

Constitutive models suitable for detailed numerical modelling of complex metal-timber connections are discussed in this Section and the approach adopted in this study to the implementation of these models for explicit solution in the finite element domain is detailed. Explicit solution of equations of motion to advance the kinematic state, rather than implicit solution through the enforcement of equilibrium by Newton-Raphson iteration, allows for more computationally efficient treatment of non-linear problems involving complex arrangements of components and contacts particularly in conjunction with large deformations and/or dynamic analyses.

Stresses $\boldsymbol{\sigma}$ and strains $\boldsymbol{\varepsilon}$ at a point can be represented on a three-dimensional cube. Material directions for the components of these stress and strain vectors are defined in Fig. 1(a).

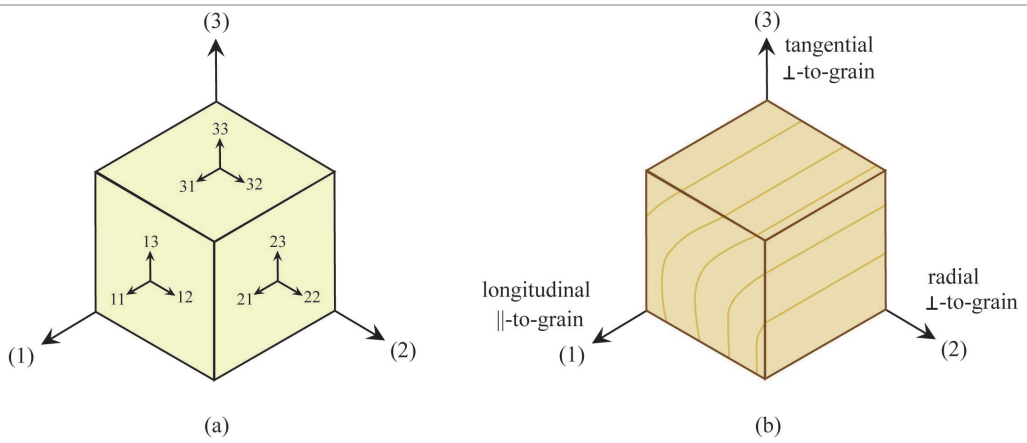

Figure 1. (a) 3D stress directions, (b) corresponding orthotropic material directions for timber

2.1 Ductile metals

Elastic behaviour of metals can be adequately modelled using the engineering constants of an isotropic elastic stiffness matrix. The Von Mises yield criterion given in Eq. (**1**) is commonly used to define the end of the elastic regime [16], [17] for most crystalline metals [41]. Yielding occurs when $f(\boldsymbol{\sigma}) \geq 0$, where σ_{eq} is the equivalent stress and σ_y is yield stress.

$$f(\boldsymbol{\sigma}) = \sqrt{\frac{1}{2}\left[\begin{matrix}(\sigma_{11}-\sigma_{22})^2+(\sigma_{22}-\sigma_{33})^2+(\sigma_{33}-\sigma_{11})^2 \\ +6(\sigma_{23}^2+\sigma_{31}^2+\sigma_{12}^2)\end{matrix}\right]} - \sigma_y = \sigma_{eq} - \sigma_y \quad (1)$$

To simulate post-elastic response in ductile metals using damage, an equivalent stress–plastic strain relationship must be defined up to fracture. Engineering stress-strain relations can be determined based on uniaxial tensile testing in each material direction and may be converted to true stress σ_T and true strain ε_T up to the onset of necking. After the onset of necking, both strain localisation and stress triaxiality must be accounted for.

Holloman extrapolation (Eq. **(2)**) is commonly used to account for strain localisation in the modelling of metallic materials [42] from the onset of necking until fracture.

$$\sigma_T = k_1(\varepsilon_T^n)^{\varepsilon_T^n} \quad (2)$$

The coefficient k_1 is calculated by substituting known values at the necking point and the superscript "n" denotes necking. The equivalent stress σ_{eq} and equivalent strain ε_{eq} are equal to σ_T and ε_T determined by uniaxial tensile testing, and from these an equivalent plastic strain component ε_{eq}^{p} can be obtained using Eq. **(3)**, where E is the Young's modulus.

$$\varepsilon_{eq}^{p} = \varepsilon_{eq} - \frac{\sigma_{eq}}{E} \tag{3}$$

To account for stress triaxiality after necking for round bar specimens, the Gromada correction factor may be applied to equivalent stress values after necking [43] with coefficients $\alpha = 0.5$ and $\beta = 0.5$ as proposed in [42].

Material softening observed in ductile metals after necking can be simulated using continuum damage modelling techniques. Damage is assumed to be initiated at the onset of necking and then evolves until stiffness reduces to zero. Damage initiation for ductile damage, due to the coalescence, nucleation and growth of voids, can be defined using an equivalent plastic strain at the onset of damage ε_{eq}^{pd}. This ε_{eq}^{pd} can be presented as a function of stress triaxiality η using Eq. **(4)** proposed by Pavlovic et al [17], where ε_T^{pn} is the true plastic strain at necking.

$$\varepsilon_{eq}^{pd}(\eta) = \varepsilon_T^{pn}\, exp\left[-1.5\left(\eta - \frac{1}{3}\right)\right] \tag{4}$$

The evolution of stiffness degradation following damage initiation can be described by a scalar damage variable D. This D is formulated in Eq. **(5)** in terms of equivalent stress σ_{eq} and of an equivalent undamaged stress $\overline{\sigma_{eq}}$ considering strain hardening behaviour without necking or softening, and then calculated for each ε_{eq}^{p}.

$$D = \left(1 - \frac{\sigma_{eq}}{\overline{\sigma_{eq}}}\right) \tag{5}$$

The crack band method [44] can be used to avoid mesh dependent strain localisation during numerical implementation by setting the fracture energy g_f equal to G_f/w. The quantity G_f, calculated using Eq. **(6)**, is the fracture energy needed to open a unit area of crack – a mesh-independent material parameter – and w is the element thickness. The total failure of an element occurs once all fracture energy is dissipated.

$$G_f = \int_{\varepsilon_{eq}^{pn}}^{\varepsilon_{eq}^{pf}} L\sigma_y d\varepsilon_{eq}^{p} = \int_{0}^{u_{eq}^{pf}} \sigma_y du_{eq}^{p} \quad (6)$$

where ε_{eq}^{pf} is the equivalent plastic strain at fracture and u_{eq}^{pf} is the equivalent plastic displacement at fracture. Equivalent plastic displacement u_{eq}^{p} can be obtained using Eq. **(7)**.

$$u_{eq}^{p} = L(\varepsilon_{eq}^{p} - \varepsilon_{eq}^{pn}) \quad (7)$$

where $\varepsilon_{eq}^{p} \geq \varepsilon_{eq}^{pn}$. Characteristic element length L is discussed further in Section 3.8 but can be taken as the typical element length for linear elements.

Shear damage initiation due to shear band localisation is represented by equivalent plastic strain at the onset of shear damage $\varepsilon_{eq,s}^{pd}$, defined as a function of shear stress ratio θ_s. Exponential softening can be used to model shear damage evolution, with multiplicative degradation simulating both ductile and shear damage simultaneously [17], [45].

2.2 Timber

The distinction between wood, timber and engineered timber is typically scale-based and relates to the hierarchical structure of the materials. Wood refers to natural material with properties characterised exclusive of larger defects such as knots. Timber refers to selected material inclusive of some larger defects. Engineered timber refers to industrially homogenised material. [46]. For the purposes of single-scale modelling; wood, timber or engineered timber as appropriate, may be idealised as homogeneous orthotropic materials. The term timber is used in the remainder of this

157 section for consistency but can be understood to apply similarly to wood and engineered timber
158 when similarly modelled as homogenous orthotropic materials with appropriately specified
159 mechanical properties.

160 The elastic behaviour of timber can be adequately modelled using the engineering constants of an
161 orthotropic elastic stiffness matrix. However, the modelling of the post-elastic behaviour is not a
162 subject of broad agreement.

163 **2.2.1 Hill criterion**

164 An extended version of the Von Mises yield criterion was proposed by Hill [20] for ductile
165 anisotropic materials. The Hill criterion is given in Eq. **(8)**, where $\sigma_{y,0}$ is the reference yield stress,
166 $\tau^0 = \sigma_{y,0}/\sqrt{3}$, and f_c and f_v are the compressive and shear strengths in the directions indicated by
167 the subscripts. For materials such as timber that lack a distinct yield point, a suitable proof stress or
168 similar reference value determined by uniaxial testing is commonly adopted for $\sigma_{y,0}$.

$$f(\boldsymbol{\sigma}) = \sqrt{\begin{bmatrix} F(\sigma_{22}-\sigma_{33})^2 + G(\sigma_{33}-\sigma_{11})^2 + H(\sigma_{11}-\sigma_{22})^2 \\ +2L\sigma_{23}^2 + 2M\sigma_{13}^2 + 2N\sigma_{12}^2 \end{bmatrix}} - \sigma_{y,\text{Hill},0} \tag{8}$$

$$F = \frac{\sigma_{y,0}^2}{2}\left(\frac{1}{f_{c,22}^2}+\frac{1}{f_{c,33}^2}-\frac{1}{f_{c,11}^2}\right), \quad G = \frac{\sigma_{y,0}^2}{2}\left(\frac{1}{f_{c,33}^2}+\frac{1}{f_{c,11}^2}-\frac{1}{f_{c,22}^2}\right),$$

$$H = \frac{\sigma_{y,0}^2}{2}\left(\frac{1}{f_{c,11}^2}+\frac{1}{f_{c,22}^2}-\frac{1}{f_{c,33}^2}\right), \quad L = \frac{3}{2}\left(\frac{\tau^0}{f_{v,23}}\right)^2, \quad M = \frac{3}{2}\left(\frac{\tau^0}{f_{v,13}}\right)^2, \quad N = \frac{3}{2}\left(\frac{\tau^0}{f_{v,12}}\right)^2$$

169 Yielding is defined when $f(\boldsymbol{\sigma}) \geq 0$. The Hill yield surface is represented in σ_{11}-σ_{22} space in
170 Fig. 2(a), using material property values from the benchmarked numerical model in Section 3.4.
171 Tension is denoted as positive. Differences in tensile and compressive strength are not
172 accommodated. Brittle failure is not considered. The yield criterion is usually applied to an elastic-
173 plastic stress-strain model including isotropic hardening. The Hill failure criterion is commonly
174 included in commercial finite element software.

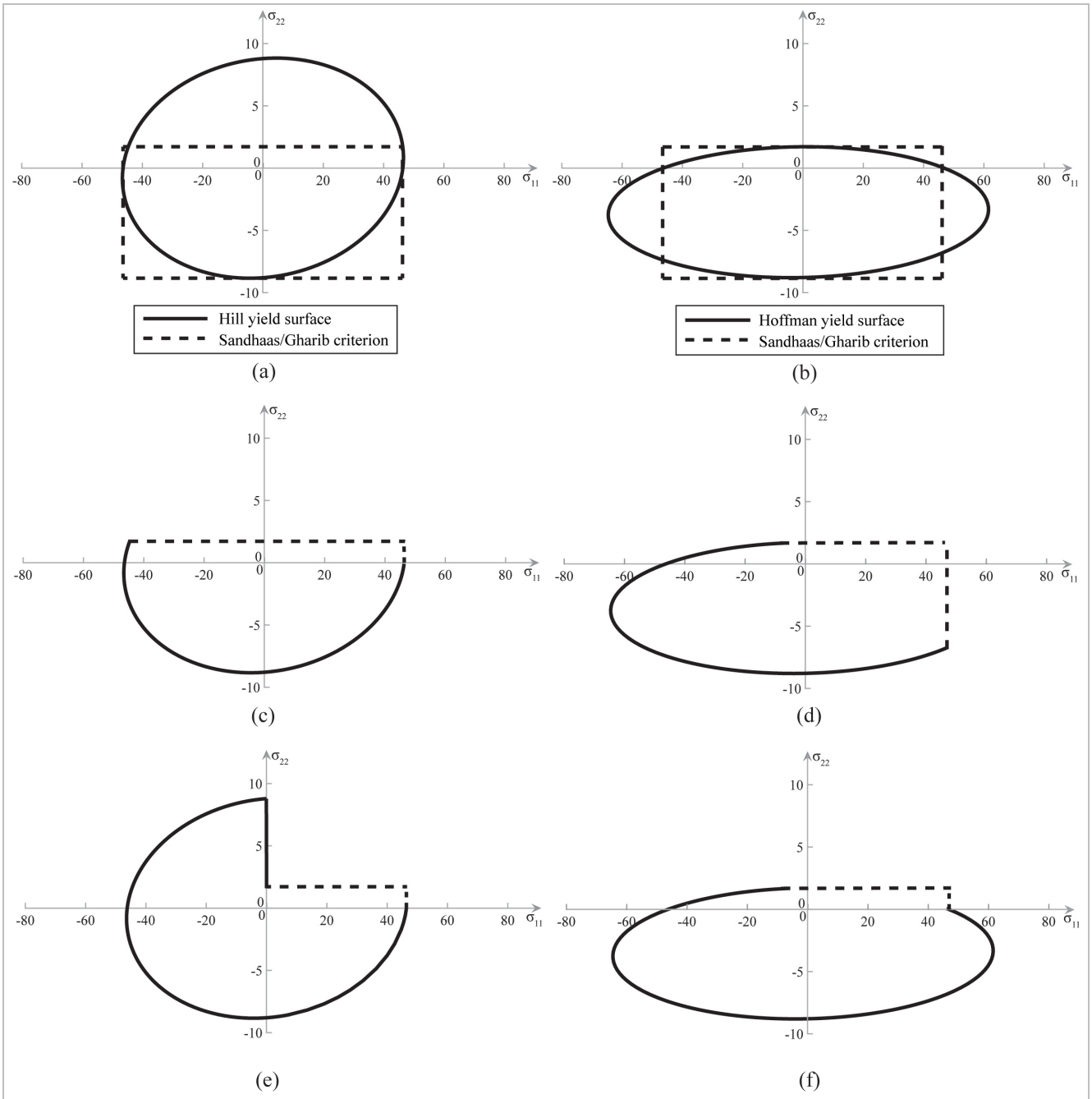

Figure 2. Yield and failure surfaces of: (a) Hill and Sandhaas/Gharib; (b) Hoffman and Sandhaas/Gharib; (c) proposed Hill-Gharib Case I; (d) proposed Hoffman-Gharib Case I; (e) proposed Hill-Gharib Case II; and (f) proposed Hoffman-Gharib Case II.

2.2.2 Hoffman criterion

The Hoffman [21] criterion (Eq. **(9)**) is an extension of the Hill criterion that accommodates differences in tensile f_t and compressive f_c material strength.

$$f(\boldsymbol{\sigma}) = \begin{bmatrix} \alpha_{23}(\sigma_{22} - \sigma_{33})^2 + \alpha_{13}(\sigma_{33} - \sigma_{11})^2 + \alpha_{12}(\sigma_{11} - \sigma_{22})^2 \\ +\alpha_{11}\sigma_{11} + \alpha_{22}\sigma_{22} + \alpha_{33}\sigma_{33} \\ +3\alpha_{44}\sigma_{12}^2 + 3\alpha_{55}\sigma_{13}^2 + 3\alpha_{66}\sigma_{23}^2 \end{bmatrix} - \sigma_{y,\mathrm{Hoff},0}^2 \quad (9)$$

$$\alpha_{12} = \frac{\sigma_{y,0}^2}{2}\left(\frac{1}{f_{c,11}f_{t,11}} + \frac{1}{f_{c,22}f_{t,22}} - \frac{1}{f_{c,33}f_{t,33}}\right),$$

$$\alpha_{23} = \frac{\sigma_{y,0}^2}{2}\left(-\frac{1}{f_{c,11}f_{t,11}} + \frac{1}{f_{c,22}f_{t,22}} + \frac{1}{f_{c,33}f_{t,33}}\right),$$

$$\alpha_{13} = \frac{\sigma_{y,0}^2}{2}\left(\frac{1}{f_{c,11}f_{t,11}} - \frac{1}{f_{c,22}f_{t,22}} + \frac{1}{f_{c,33}f_{t,33}}\right),$$

$$\alpha_{11} = \sigma_{y,0}^2\left(\frac{f_{c,11}-f_{t,11}}{f_{c,11}f_{t,11}}\right),\ \alpha_{22} = \sigma_{y,0}^2\left(\frac{f_{c,22}-f_{t,22}}{f_{c,22}f_{t,22}}\right),\ \alpha_{33} = \sigma_{y,0}^2\left(\frac{f_{c,33}-f_{t,33}}{f_{c,33}f_{t,33}}\right),$$

$$\alpha_{44} = \frac{\sigma_{y,0}^2}{3f_{v,12}^2},\ \alpha_{55} = \frac{\sigma_{y,0}^2}{3f_{v,13}^2},\ \alpha_{66} = \frac{\sigma_{y,0}^2}{3f_{v,23}^2}$$

Yielding is defined when $f(\boldsymbol{\sigma}) \geq 0$. The Hoffmann yield surface is represented in σ_{11}-σ_{22} space in Fig. 2(b). Unlike Hill, the influence of hydrostatic stresses is considered, although the actual contribution of hydrostatic stresses to timber failure is unclear [29]. The yield criterion is usually applied to an elastic-plastic model including isotropic hardening. The Hoffmann criterion is not commonly included in commercial finite element software.

2.2.2.1 Formulation for explicit solution in finite element domain

Subroutines implementing the Hoffman criterion for implicit solution in the finite element domain have been presented previously [25], [26]. A new user subroutine was developed in Fortran language as part of this study in order to use the explicit solver function of ABAQUS/Explicit that is better suited to analysing complex problems including interactions, softening and dynamic effects.

Implicit solution in the finite element domain typically applies load in small time increments Δt and uses the backward Euler method to approximate the solution at time $t + \Delta t$ iteratively, based on values at t and $t + \Delta t$. Explicit solution requires the forward Euler method, whereby quantities at time $t + \Delta t$ are approximated using values at t explicitly. The numerical formulation developed in

this study for explicit solution is discussed in detail below. All calculations are performed at each integration point.

At the beginning of an increment, at time t, variables $\boldsymbol{\varepsilon}_t$, $\boldsymbol{\varepsilon}_{\Delta t}$, $\varepsilon^p_{eq,Hoff,t}$, $\sigma_{y,0,t}$ and $\boldsymbol{\sigma}_t$ are known. Strains and stresses at $t + \Delta t$ can be expressed as given in Eq. **(10)** and Eq. **(11)** respectively.

$$\boldsymbol{\varepsilon}_{t+\Delta t} = \boldsymbol{\varepsilon}_t + \boldsymbol{\varepsilon}_{\Delta t} \tag{10}$$

$$\boldsymbol{\sigma}_{t+\Delta t} = \boldsymbol{\sigma}_t + \boldsymbol{\sigma}_{\Delta t} \tag{11}$$

$$\boldsymbol{\sigma}_{\Delta t} = \boldsymbol{K}_E \boldsymbol{\varepsilon}^e_{\Delta t} \tag{12}$$

where $\boldsymbol{K}_E$ is the elastic stiffness matrix. The strain increment $\boldsymbol{\varepsilon}_{\Delta t}$ can be decomposed into elastic $\boldsymbol{\varepsilon}^e_{\Delta t}$ and plastic $\boldsymbol{\varepsilon}^p_{\Delta t}$ components as shown in Eq. **(13)**.

$$\boldsymbol{\varepsilon}_{\Delta t} = \boldsymbol{\varepsilon}^e_{\Delta t} + \boldsymbol{\varepsilon}^p_{\Delta t} \tag{13}$$

Substituting Eq. **(13)** into Eq. **(11)** and rearranging provides:

$$\boldsymbol{\sigma}_{t+\Delta t} = \boldsymbol{\sigma}_t + \boldsymbol{K}_E(\boldsymbol{\varepsilon}_{\Delta t} - \boldsymbol{\varepsilon}^p_{\Delta t}) \tag{14}$$

A trial stress considering no plastic behaviour can be obtained using Eq. **(15)**.

$$\boldsymbol{\sigma}^{\boldsymbol{Trial}}_{t+\Delta t} = \boldsymbol{\sigma}_t + \boldsymbol{K}_E \boldsymbol{\varepsilon}_{\Delta t} \tag{15}$$

Substituting Eq. **(15)** into Eq. **(14)** gives:

$$\boldsymbol{\sigma}_{t+\Delta t} = \boldsymbol{\sigma}^{Trial}_{t+\Delta t} - \boldsymbol{K}_E \boldsymbol{\varepsilon}^p_{\Delta t} \tag{16}$$

Trial stresses are first determined to check whether yielding has occurred based on Eq. **(9)**. If no yielding exists, then $\boldsymbol{\varepsilon}^p_{\Delta t} = 0$ and $\boldsymbol{\sigma}_{t+\Delta t} = \boldsymbol{\sigma}^{Trial}_{t+\Delta t}$. Therefore, the stresses at time $t + \Delta t$ can be directly found from the trial stresses. If yielding occurs, the $\boldsymbol{\sigma}^{Trial}_{t+\Delta t}$ needs to be corrected as shown in Eq. **(16)**. This process is the return mapping algorithm. Accordingly, $\boldsymbol{\varepsilon}^p_{\Delta t}$ is estimated from the

associated flow rule (Eq. **(17)**), which postulates that $\boldsymbol{\varepsilon}^p_{\Delta t}$ and the normal to the yield surface have the same direction.

$$\boldsymbol{\varepsilon}^p_{\Delta t} = \lambda_{\Delta t}\left(\frac{\partial f(\boldsymbol{\sigma}_t)}{\partial \boldsymbol{\sigma}_t}\right) \tag{17}$$

The parameter λ is a hardening parameter and is greater than zero. This λ and $f(\boldsymbol{\sigma})$ must conform to the Karush-Kuhn-Tucker (KKT) conditions. The first condition requires that, during loading and unloading, plastic strain increment is equal to or greater than zero. The second requires that the stress state must lie on, or within, the yield surface. These KKT conditions are given in Eq. **(18)**.

$$\lambda_{\Delta t} \geq 0, \qquad f(\boldsymbol{\sigma}_{t+\Delta t}) \leq 0, \qquad \lambda_{\Delta t} f(\boldsymbol{\sigma}_{t+\Delta t}) = 0 \tag{18}$$

A consequence of the third condition is Prager's consistency condition, which can be utilized to eliminate the unknown parameter, $\lambda_{\Delta t}$. This condition asserts that the stresses must lie on the yield surface during plastic deformations and is formulated as:

$$f(\boldsymbol{\sigma}_{t+\Delta t}) = f(\boldsymbol{\sigma}_t) + df \tag{19}$$

where $f(\boldsymbol{\sigma}_{t+\Delta t}) = 0 \; and \; f(\boldsymbol{\sigma}_t) = 0$. This leads to Eq. **(20)**,

$$df = \left(\frac{\partial f(\boldsymbol{\sigma}_t)}{\partial \boldsymbol{\sigma}_t}\right)^T \boldsymbol{\sigma}_{\Delta t} + \left(\frac{\partial f(\boldsymbol{\sigma}_t)}{\partial \varepsilon^p_{eq,Hoff,t}}\right) \varepsilon^p_{eq,Hoff,\Delta t} = 0 \tag{20}$$

A reference yield stress, considering hardening behaviour, can be expressed as:

$$\sigma_{y,0,t+\Delta t} = \sigma_{y,0,t} + H\varepsilon^p_{eq,Hoff,\Delta t}, \qquad H = \frac{\Delta \sigma_y}{\Delta \varepsilon^p_{eq,Hoff}} \tag{21}$$

with $\varepsilon^p_{eq,Hoff,\Delta t}$ defined following [25], [47], [48], [49] as given in Eq. **(22)**:

$$\varepsilon^p_{eq,\mathrm{Hoff},\Delta t} = \lambda_{\Delta t} h, \qquad h = \sqrt{\frac{2}{3}\left(\frac{\partial f(\boldsymbol{\sigma}_t)}{\partial \boldsymbol{\sigma}_t}\right)^T \left(\frac{\partial f(\boldsymbol{\sigma}_t)}{\partial \boldsymbol{\sigma}_t}\right)} \tag{22}$$

Solving Eq. **(20)** using Eq. **(21)** and Eq. **(22)** gives Eq. **(23)**, a solution to $\lambda_{\Delta t}$:

$$\lambda_{\Delta t} = \frac{\left(\frac{\partial f(\boldsymbol{\sigma}_t)}{\partial \boldsymbol{\sigma}_t}\right)^T \boldsymbol{K}_E \, \boldsymbol{\varepsilon}_{\Delta t}}{\left(\frac{\partial f(\boldsymbol{\sigma}_t)}{\partial \boldsymbol{\sigma}_t}\right)^T \boldsymbol{K}_E \left(\frac{\partial f(\boldsymbol{\sigma}_t)}{\partial \boldsymbol{\sigma}_t}\right) + 2\sigma_{y,0,t} H h} \tag{23}$$

A solution to the stress vector at time $t + \Delta t$ can then be found using Eq. **(16)** and $\boldsymbol{\varepsilon}_{t+\Delta t}$, $\varepsilon^p_{eq,Hoff,t+\Delta t}$, and $\boldsymbol{\sigma}_{t+\Delta t}$ are updated at the end of the increment for each integration point. The specific internal energy $I_{t+\Delta t}$ and the specific plastic work $W^p_{t+\Delta t}$ can be estimated as presented in Eq. **(24)** and Eq. **(25)**, where ρ is material density:

$$I_{t+\Delta t} = I_t + \frac{\sum 0.5(\boldsymbol{\sigma}_t + \boldsymbol{\sigma}_{t+\Delta t})\boldsymbol{\varepsilon}_{\Delta t}}{\rho} \tag{24}$$

$$W^p_{t+\Delta t} = W^p_t + \frac{0.5(\sigma_{y,0,t} + \sigma_{y,0,t+\Delta t})\varepsilon^p_{eq,\mathrm{Hoff},\Delta t}}{\rho} \tag{25}$$

2.2.3 Sandhaas model

A constitutive model including a multi-surface failure criterion considering both compressive and tensile behaviour of timber is proposed by Sandhaas et al [34]. A detailed discussion of this model and the constituent formulae can be found in [34]. The failure criterion has eight different failure regions based on maximum principal stress theory as given in Eqs. **(26)-(33)**. Yielding occurs when $F_c(\sigma) \geq 1$ and brittle failure occurs when $F_t(\sigma) \geq 1$ or $F_v(\sigma) \geq 1$.

$$F_{t,11}(\sigma) = \frac{\sigma_{11}}{f_{t,11}};\ \sigma_{11} \geq 0 \tag{26}$$

$$F_{c,11}(\sigma) = \frac{-\sigma_{11}}{f_{c,11}};\ \sigma_{11} < 0 \tag{27}$$

$$F_{t,22}(\sigma) = \frac{\sigma^2_{22}}{f^2_{t,22}} + \frac{\sigma^2_{12}}{f^2_{v,12}} + \frac{\sigma^2_{23}}{f^2_{v,23}};\ \sigma_{22} \geq 0 \tag{28}$$

$$F_{c,22}(\sigma) = \frac{-\sigma_{22}}{f_{c,22}}; \sigma_{22} < 0 \quad (29)$$

$$F_{v,12}(\sigma) = \frac{\sigma_{12}^2}{f_{v,12}^2} + \frac{\sigma_{23}^2}{f_{v,23}^2}; \ \sigma_{22} < 0 \quad (30)$$

$$F_{t,33}(\sigma) = \frac{\sigma_{33}^2}{f_{t,33}^2} + \frac{\sigma_{13}^2}{f_{v,13}^2} + \frac{\sigma_{23}^2}{f_{v,23}^2}; \ \sigma_{33} \geq 0 \quad (31)$$

$$F_{c,33}(\sigma) = \frac{-\sigma_{33}}{f_{c,22}}; \ \sigma_{33} < 0 \quad (32)$$

$$F_{v,13}(\sigma) = \frac{\sigma_{13}^2}{f_{v,13}^2} + \frac{\sigma_{23}^2}{f_{v,23}^2}; \ \sigma_{33} < 0 \quad (33)$$

The Sandhaas failure surface is represented in σ_{11}-σ_{22} space in Fig. 2(a) and (b) for comparison with the Hill and Hoffmann yield surfaces respectively. The criterion is used to specify the initiation of yielding and damage, with continuum damage modelling techniques then used to simulate the damage evolution. Bilinear stress-strain relationships adopted by Sandhaas are presented in Fig. 3(a) and (b) for compression and tension respectively.

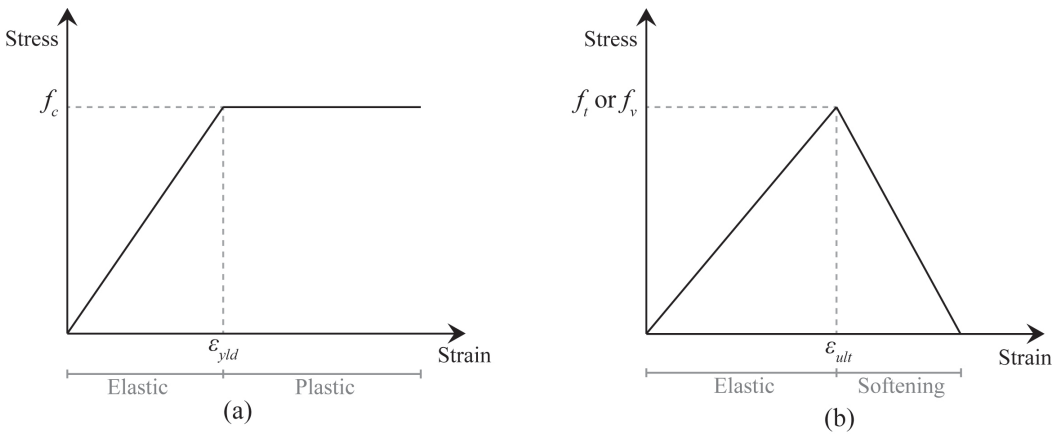

Figure 3. (a) Elastic-perfectly plastic and (b) elastic-softening stress-strain relationships adopted by Sandhaas

Damage variables are embedded in the compliance matrix to derive a damaged stiffness matrix $\boldsymbol{K}^{dam}$, with Eq. **(34)** used to obtain stresses [34]. The fracture energy-based crack band method is used to avoid mesh dependency due to softening during brittle damage.

$$\boldsymbol{\sigma}_{\boldsymbol{t+\Delta t}} = \boldsymbol{K}^{dam}\boldsymbol{\varepsilon}_{t+\Delta t} \quad (34)$$

The Sandhaas model has previously been implemented for implicit solution using the backward-Euler method. A new subroutine implementing this model for explicit solution using the forward Euler method, was developed for this study. The formulae of the failure criterion and damage variables remain unchanged, but the iterative process and the requirement of a Jacobian matrix for tangent stiffness are circumvented by employing a two-state architecture that incorporates old and new arrays. A summary of the numerical procedure adopted is presented in Fig. 4.

Element deletion is added in the new subroutine, with the deletion parameter set to active when damage variables reach a value of 0.99995, i.e., closely approaching a value of unity, in order to avoid numerical instability. Viscous regularisation, which is often used to improve the convergence of implicit solution, is not required for explicit solution.

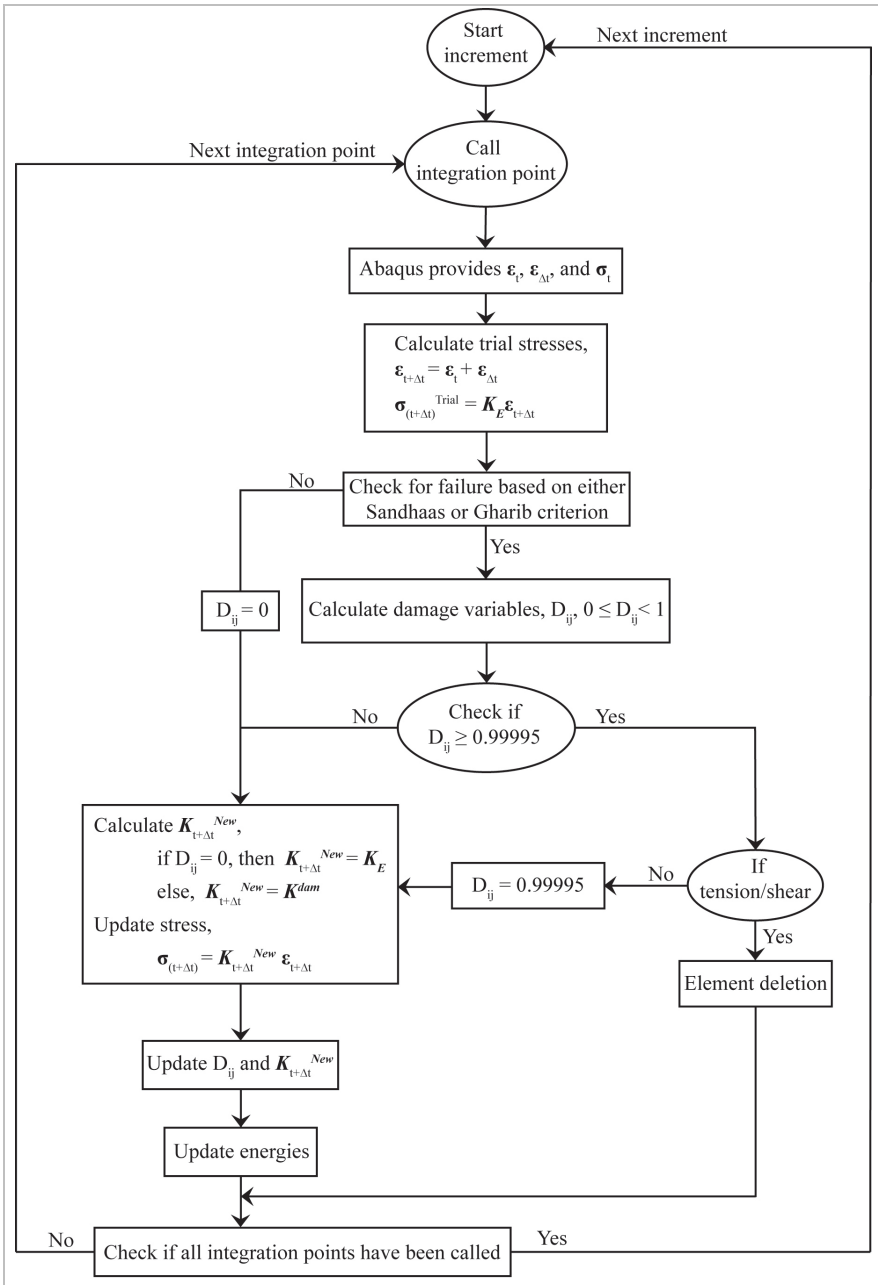

Figure 4. Numerical approach adopted for implementation of the Sandhaas and Gharib constitutive models

2.2.4 Gharib model

A constitutive model adopting the Sandhaas failure criterion supplemented with well-defined hardening, softening and brittle damage responses for timber has been proposed by Gharib et al. [36]. The Sandhaas failure criterion is used to specify the initiation of yielding and damage, with continuum damage modelling techniques used to simulate the damage evolution. The general form of the multi-linear stress-strain relationship adopted in the Gharib model is presented in Fig. 5. This

model is able to represent more varied stress-strain responses than that adopted by Sandhaas, including plastic hardening and bi-linear softening. The introduction of the residual region to the bilinear-softening branch improves numerical stability.

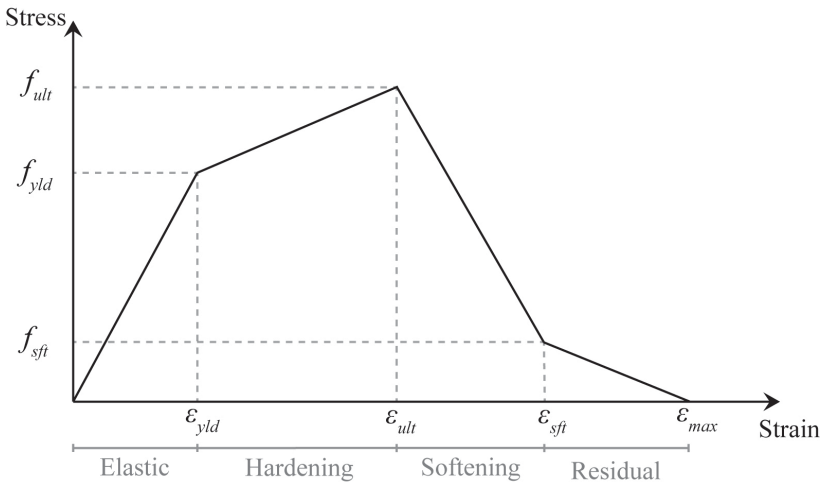

Figure 5. Reference stress-strain relationship adopted for timber in the Gharib model

Damage variables that account for hardening, softening and residual regimes are different to those of Sandhaas, but similarly embedded in the compliance matrix. A detailed discussion of this model including damage variables can be found in [36]. The fracture energy-based crack band method is employed to simulate brittle damage. The Gharib model has previously been implemented for implicit solution using the backward-Euler method. A new subroutine implementing this model for explicit solution, using the forward Euler method, was developed in this study. This subroutine incorporates element deletion as described in Section 2.2.3. A summary of the numerical procedure adopted is shown in Fig. 4.

2.2.5 Proposed composite failure criteria

Constitutive models adopting maximum principal stress theory based failure criteria may not adequately represent ductile failure behaviour, particularly under bi-axial or tri-axial stress states, as has been observed experimentally [18]. Conversely, constitutive models adopting elliptical yield surfaces have been shown to adequately represent ductile behaviour [27], but are not capable of modelling brittle failure. Therefore, two new constitutive models adopting composite failure criteria

that combine maximum principal stress theory piecewise with an elliptical yield surface, are considered.

2.2.5.1 Hill-Gharib model

A composite Hill-Gharib model is proposed whereby yielding is defined by the Hill yield criterion followed by isotropic hardening; and brittle failure is defined by maximum principal stress criterion followed by continuum damage modelling after Gharib. The Gharib model is selected over the Sandhaas model for its well-defined hardening, softening and damage responses, and numerical stability. A new subroutine implementing the proposed Hill-Gharib model for explicit solution using the forward-Euler method was developed for this study. A flowchart for the implementation of the proposed criterion is depicted in Fig. 6, combining the numerical procedures set out in Section 2.2.2 and Section 2.2.4. However, $\frac{\partial f(\boldsymbol{\sigma}_t)}{\partial \boldsymbol{\sigma}_t}$ and associated calculations differ somewhat from those described in Section 2.2.2 with $\frac{\partial f(\boldsymbol{\sigma}_t)}{\partial \boldsymbol{\sigma}_t}$ determined following Eq. (**35**). The stress-strain relationship for compression is an elastic-plastic model with isotropic hardening, while the relationship for tension is an elastic-softening-residual model.

$$\frac{\partial f(\boldsymbol{\sigma}_t)}{\partial \boldsymbol{\sigma}_t} = \frac{1}{f(\boldsymbol{\sigma}_t)} \begin{Bmatrix} -G\left(\sigma_{33,t} - \sigma_{11,t}\right) + H\left(\sigma_{11,t} - \sigma_{22t}\right) \\ F\left(\sigma_{22,t} - \sigma_{33,t}\right) - H\left(\sigma_{11,t} - \sigma_{22,t}\right) \\ -F\left(\sigma_{22,t} - \sigma_{33,t}\right) + G\left(\sigma_{33,t} - \sigma_{11,t}\right) \\ 2N\sigma_{12,t} \\ 2L\sigma_{23,t} \\ 2M\sigma_{13,t} \end{Bmatrix} \tag{35}$$

Two separate cases were defined following the conditions given in Box "A" in Fig. 6. Case I allows tensile or shear failure if at least one normal stress component is in tension. However, the crack band model is effective when only one failure band is dominant at a time [34], [36]. Abrupt artificial softening and energy generation can occur when failing elements are unable to adequately redistribute load to adjacent elements, resulting in the formation of multiple failure bands in neighbouring regions. To limit the occurrence of multiple failure bands, a stricter condition was

299 defined for Case II, permitting tensile failure only if all three normal stress components are in
300 tension. The Case II condition is unrealistic when applied to macro-level situations, but when the
301 condition is applied at the micro- (i.e., element) level in the finite element analysis, the macro-level
302 response may remain realistic. Other techniques such as non-local formulations [50] can alternatively
303 be used at the expense of high computational effort and complex formulations. The two cases lead to
304 two distinct failure surfaces and thus result in two different constitutive models. The cases do not
305 interact and analyses are conducted separately for each case. The failure surface of the proposed
306 composite failure criterion is represented in σ_{11}-σ_{22} space in Fig. 2(c) and (e) for Case I and Case II
307 respectively. The solid line indicates the portion of the surface governed by yielding while the
308 dashed line indicates that governed by brittle failure. Note that when the yield surface expands with
309 isotropic hardening, failure modes in quadrants I and III may transition from yielding to brittle
310 failure.

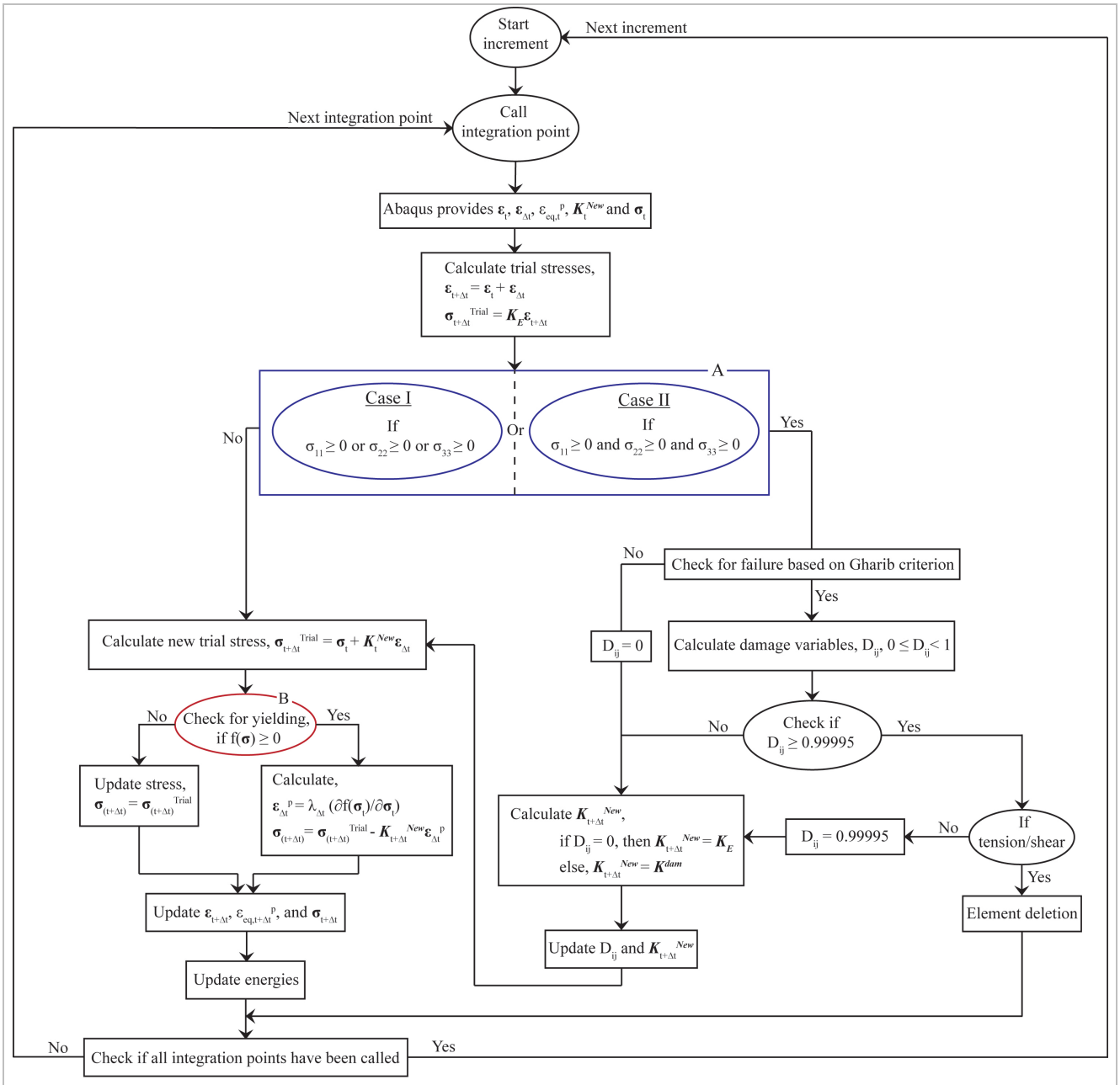

Figure 6. Numerical approach adopted for implementation of the proposed Hill-Gharib and Hoffman-Gharib failure criteria

2.2.5.2 Hoffman-Gharib model

A composite Hoffman-Gharib model is similarly proposed whereby yielding is defined by the Hoffmann yield criterion followed by isotropic hardening; and brittle failure is defined by maximum principal stress criterion followed by continuum damage modelling after Gharib. Separate Case I and Case II tension failure conditions are defined in an analogous manner to the Hoffmann-Gharib criterion described in Section 2.2.5.1. The failure surface of the proposed composite model is

presented in Fig. 2(d) and (f) for Case I and Case II respectively. A new subroutine implementing the proposed Hill-Gharib model for explicit solution using the forward-Euler method was developed for this study. The numerical procedure for implementation is similar to that described in Section 2.2.5.1 except that the Hill criterion is replaced by the Hoffman criterion for $f(\boldsymbol{\sigma})$ in circle "B" in Figure 6.

3 Numerical modelling of a bolted T-section beam-column connection

This Section presents detailed numerical modelling of a multi-material steel, aluminium and LVL timber beam-column connection under large deformations in shear and moment dominated tests. The detailed numerical modelling synthesises key techniques and provides detailed guidance on their application to the simulation of complex timber-metal connections through large deformations. The numerical model is benchmarked against empirical results reported in the literature. The numerical model is then used to compare the different constitutive models for timber detailed in Section 2.

3.1 Modelled connection

A concealed T-shaped aluminium beam-column connector with steel bolts and dowels tested by Masaeli et al [51] was chosen as an empirical benchmark for the numerical model based on the complexity of the tested arrangement, the high quality of the experimental investigation and the detailed reporting of the test parameters and results. Detailed design of the tested connection and full experimental results are given in [51]; necessary properties and results are reproduced in this paper.

The tested T-connector was fabricated from AW 6005-A aluminium alloy extruded sections and the beams and columns from Douglas fir LVL timber. Beam and column sections were 600×252 mm^2 and 360×360 mm^2 respectively. A schematic of the full two-sided connection concept is depicted in Fig. 7. Each beam is connected to a T-connector using one row of ten 16 mm S355 steel dowels. T-connectors are located flush to the column face on each side and connected by two rows of six 16 mm diameter grade 8.8 M16 bolts through the flange. Representative single-sided connection arrangements were tested in moment and shear dominated arrangements by Masaeli et al [51].

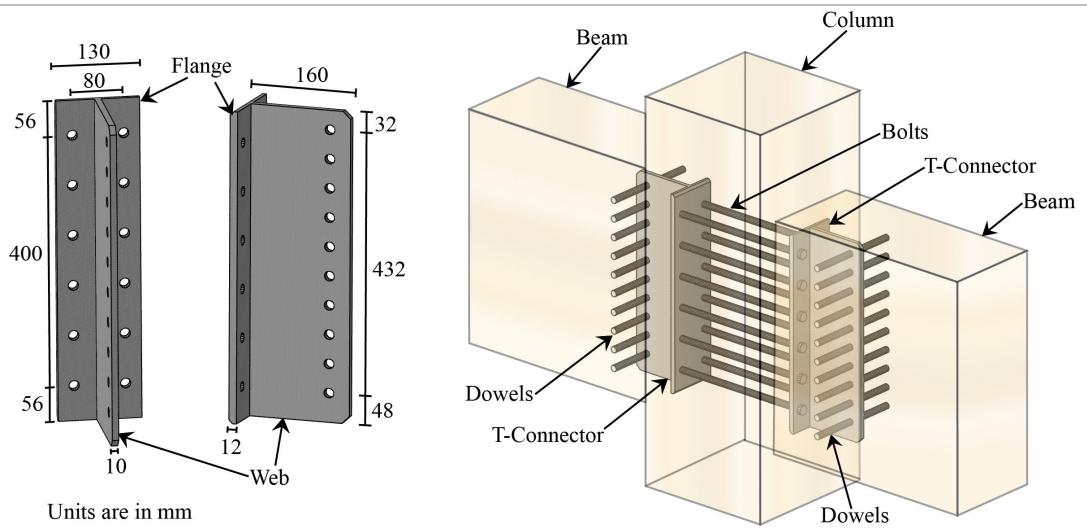

Figure 7. Details of the "T-connector", redrawn after Masaeli et al. [51]

The tested moment and shear arrangements are modelled numerically here in the commercially available finite element (FE) software package ABAQUS [45]. Each part was drawn individually and subsequently assembled to form the complete timber beam-column connection. Two modifications to the geometry reported in [51] were adopted to improve model performance.

1. Corners were modelled with 8 mm chamfers to avoid stress singularities during contact which may reach infinity [45] and adversely influence stress-based failure criteria.
2. Timber stiffness near a slot or hole made in timber has been observed to be weaker than the bulk stiffness [52], [53]. The tested connection [51] includes a recess cut to conceal the flange of the T-connection at the beam end. Numerical modelling of the resulting contact conditions, where both timber-timber and timber-metal contacts exist within the same surface, can produce spurious results. Therefore, a 4 mm gap between the column face and the beam end was modelled as a convenient alternative representation of the locally reduced timber cross-section. This gap also provides clearance between the bolt nut and the beam end, helping avoid initial mesh penetrations. A preliminary study investigating the effect of including such a gap for the purposes of modelling is presented in [54].

3.2 Mesh

Despite high accuracy, full integration elements are computationally expensive and may suffer from shear locking when subjected to bending. Therefore, an 8-node linear hexahedral element with reduced integration (C3D8R) was chosen for all the parts in the assembly. C3D8R elements have only one integration point at the centre, so are unable to capture certain deformation modes, especially near the edges of the element under bending. This leads to zero energy deformation modes or hour-glassing, where elements distort without any strains calculated at the integration point. To overcome hour-glassing, an artificial stiffness can be provided by an inbuilt relax-stiffness hourglass option. However, in order that this artificial stiffness not adversely affect the model overall, the artificial energy of the system should be maintained at less than 5% of the internal energy through mesh refinements [45]. Since C3D8R has only one integration point, a minimum of four through-thickness elements in a part are required to produce reasonably accurate results. Partitions were made for each component in the assembly to guide the meshing algorithm in obtaining an undistorted compatible mesh. A mesh sensitivity analysis for each part was also performed to obtain an optimum number of elements whilst maintaining suitable accuracy.

3.3 Contacts

Element-based surfaces were manually selected and paired using the general contact algorithm. A balanced main-secondary surface weighting with penalty contact enforcement was employed. Sliding behaviour of contacts was defined employing a common friction coefficient of 0.3, considering all the surfaces and numerical stability [55], [56], [57], [58]. To simulate large deformations, a finite sliding formulation was also applied. Normal behaviour of bolt-timber and dowel-timber contacts was defined using a generalised Lamé function (Eq. **(36)**) proposed by Dorn [59], [35] to account for material softening observed near timber holes. This function characterises the pressure-overclosure relationship or resistance to penetration adopting a non-linear softening model.

$$\left(\frac{U}{U_0}\right)^{n_u} + \left(\frac{\sigma_0 - \sigma_{cp}}{\sigma_0}\right)^{n_\sigma} = 1 \quad (36)$$

where U is the contact overclosure, U_0 is the maximum contact overclosure, σ_0 is the maximum compressive strength of timber and σ_{cp} is the contact pressure. The Lamé parameters adopted here are shown in Table 1.

Table 1. Lamé parameters for steel-timber normal contact [35]

σ_0	n_σ	U_0	n_u
46.4 N mm^{-2}	3.9	0.45 mm	1.1

3.4 Material properties

The constitutive and damage modelling approaches used in this study are set out in detail for metals in Section 2.1 and for timber in Section 2.2. The values adopted for the benchmarked numerical model are summarised in Table 2, Table 3, Table 4 and Table 5, and are described in this Section. Density ρ, Young's modulus E, Poisson's ratio υ, shear modulus G, engineering stress at necking σ_E^n and strength f values are reported by Masaeli et al [51], and engineering strains at necking ε_E^n for metals were obtained from the wider literature [16], [60].

3.4.1 Metals

Equivalent stress-strain relationships, accounting for strain localisation and stress triaxiality, are used to define plastic yielding, strain hardening and ductile damage. Necessary isotropic material properties are summarised in Table 2. The true fracture strain ε_{Tf} values were calculated from experimental data in [51]. Engineering stress-strain relations were determined for each material up to the necking point. These engineering relations were then converted to true stress-strain relations and extrapolated up to ε_{Tf} using the Holloman model.

Table 2. Material properties of metals [22], [51], [61]

Parameter	Unit	Grade 8.8	S355	AW 6005-A
ρ	kg m^{-3}	8050	8050	2710
E	GPa	207	209	70
υ		0.3	0.3	0.3
σ_y	MPa	861	556	187
σ_E^n	MPa	956	597	221
ε_E^n		0.090	0.100	0.055
ε_{Tf}		1.030	0.900	1.100

405

406 The relationships applied for the damage initiation (Eq. **(4)**) and damage evolution are plotted in
407 Fig. 8. The damaged and undamaged equivalent stress-strain relationships are shown in Fig. 9 and
408 were employed as inputs to define the yielding, necking and damage evolution. A constant θ_s= 1.732
409 and ε_{eq}^p= 0.095 at failure zones of grade 8.8 metals is assumed following [17]. Damage evolution is
410 characterised by an exponential softening law parameter of 0.7 [17] and u_{eq}^{pf} of 0.19 mm (Eq. **(7)**).
411 Shear damage was not included for aluminium and S355 steel due to lack of data.

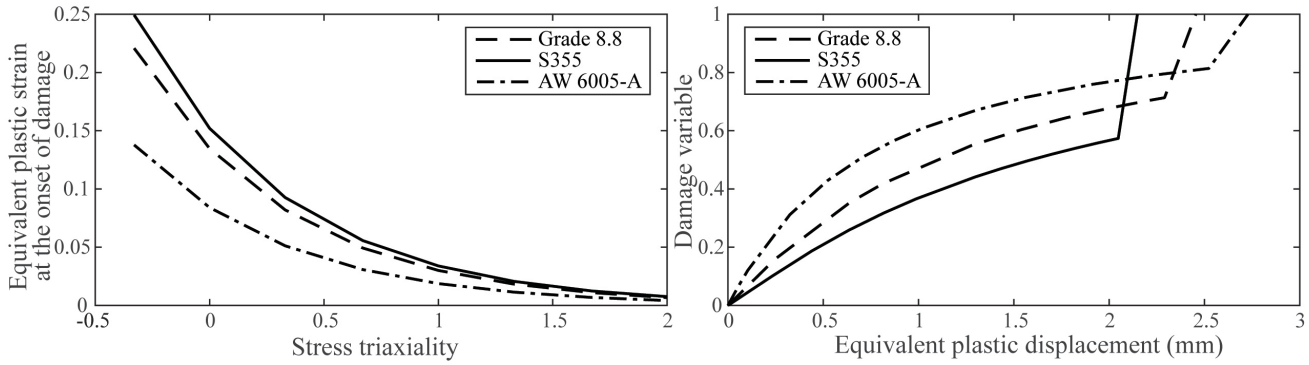

412

413 **Figure 8. (a) Damage initiation, (b) damage evolution**

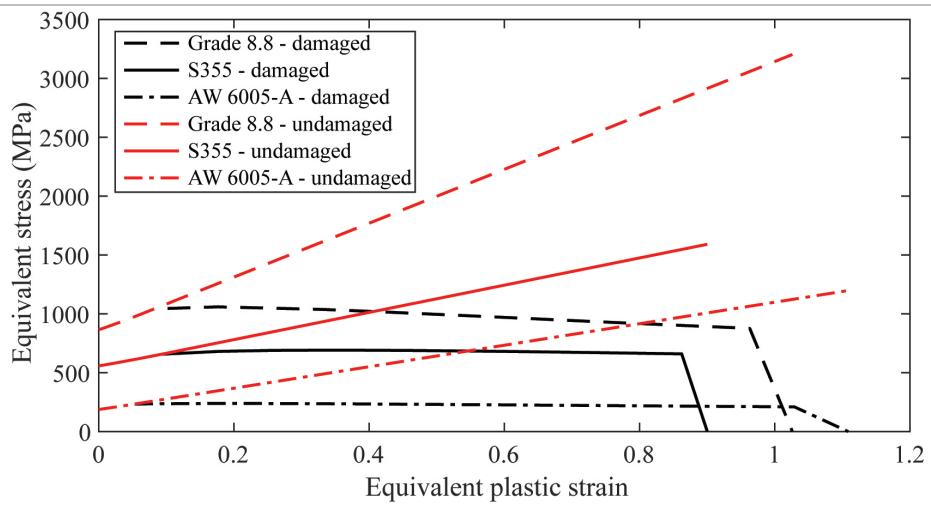

Figure 9. Equivalent stress vs equivalent plastic strain

3.4.2 LVL Timber

Material properties for LVL timber are given in Table 3 and Table 4, where f_c, f_t and f_v are strengths in compression, tension and shear respectively. Orthotropic material models with homogeneous behaviour were considered. Orthotropic material directions aligned with the stress tensor are depicted in Fig. 1(b).

Table 3. LVL stiffness properties [12], [51]

Density [kgm^{-3}]	Elastic modulus [N mm^{-2}]			Poisson's ratio			Shear modulus [N mm^{-2}]		
ρ	E_{11}	E_{22}	E_{33}	ν_{12}	ν_{13}	ν_{23}	G_{12}	G_{13}	G_{23}
592.5	15500	470	470	0.37	0.37	0.38	660	660	132

Table 4. LVL strength properties [12], [51]

Compressive strength [N mm^{-2}]			Tensile strength [N mm^{-2}]			Shear strength [N mm^{-2}]		
$f_{c,11}$	$f_{c,22}$	$f_{c,33}$	$f_{t,11}$	$f_{t,22}$	$f_{t,33}$	$f_{v,12}$	$f_{v,13}$	$f_{v,23}$
46.4	8.8	8.8	46.4	1.7	1.7	7	7	1.4

The G_f values applied in this study are presented in Table 5 and were taken from experimental studies in the literature [34], [61], [62]. An elastic-plastic hardening stress-strain relationship for

compression and a linear elastic-softening relationship for tension were applied based on these material properties, including a residual stress $f_{sft} = 0.25\, f_{ult}$ for the Gharib model.

Table 5. LVL fracture energies [34], [61], [62]

Fracture energy [N mm^{-1}]					
$G_{f,t,11}$	$G_{f,t,22}$	$G_{f,t,33}$	$G_{f,v,12}$	$G_{f,v,13}$	$G_{f,v,23}$
116	1.17	1.17	6.4	6.4	5.07

3.5 Boundary Conditions

Boundary conditions simulating the support and loading conditions reported in [51] for moment and shear tests of a one-sided T-connection are shown in Fig. 10(a) and (b) respectively, in addition to those taking advantage of symmetry.

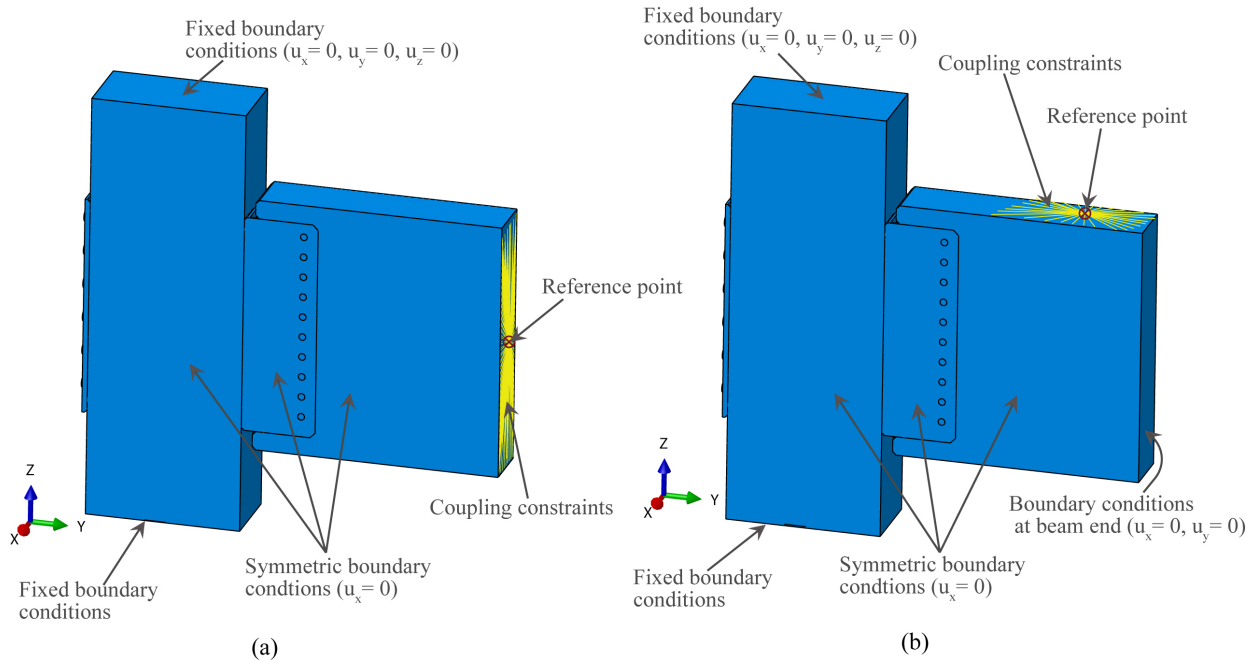

Figure 10. Boundary conditions of the (a) moment and (b) shear tests

Continuity of columns is simulated by fixed boundary conditions top and bottom at 250 mm from the beam faces. Nodes already involved in contacts and constraint definitions were excluded from the symmetric boundary conditions. Loading is applied to a reference point attached to the beam using coupling constraints with continuum distribution as presented in Fig. 10. This coupling technique constrains the degrees of freedom of the connecting surface to the degrees of freedom of the

reference point by distributing the applied load on the reference point in an average sense to the connecting surface, maintaining continuum behaviour. Loading was applied under displacement control.

3.6 Loading

Explicit solution requires very small time increments to directly simulate quasi-static loading while maintaining acceptably low kinetic energy in the modelled system. This is often computationally impractical, even with high-performance computing. One method to reduce computational effort is to increase the load-rate of the problem while maintaining acceptably low kinetic energy, typically by trial-and-error, following an initial estimate that loading time is >300% the natural period of the system and the load-rate is <1% of the wave speeds of the materials [45]. Another method is to use mass-scaling to artificially increase the time increment size, thereby reducing the total number of increments. An initial sensitivity analysis was performed to determine suitable values of mass-scaling and load-rate to achieve a kinetic energy <5% of total energy whilst minimising computational effort. A load-rate of 0.25 m s^{-1} and a mass scaling factor of 10, corresponding to a time increment of $6.208e^{-07}$ seconds, were selected and adopted throughout. Details of the sensitivity analysis are reported in [54].

3.7 Analyses and Discussion

3.7.1 Moment Simulation

Fig. 11 compares the modelled moment-rotation responses with the experimental moment test results in [51]. The moment-rotation curve from the numerical model with the Hill criterion for timber accurately captures the experimental curve including the failure mode. The Hoffman criterion, on the other hand, over-predicts the average peak moment by approximately 8% and under-predicts the average rotation prior to softening by 19%, but accurately captures the failure mode. This increased resistance may be due to the larger yield surface of the Hoffman criterion in the compression

quadrants. Both Sandhaas and Gharib models greatly under-predict the peak moment and rotation values. This is primarily because rapid damage progression occurs once element failure due to tensile fracture starts to develop, producing kinetic energy and hence inaccurate results. Simulated failure modes exhibited shear fracture due to compression for both criteria, leading to premature failure in the computational model.

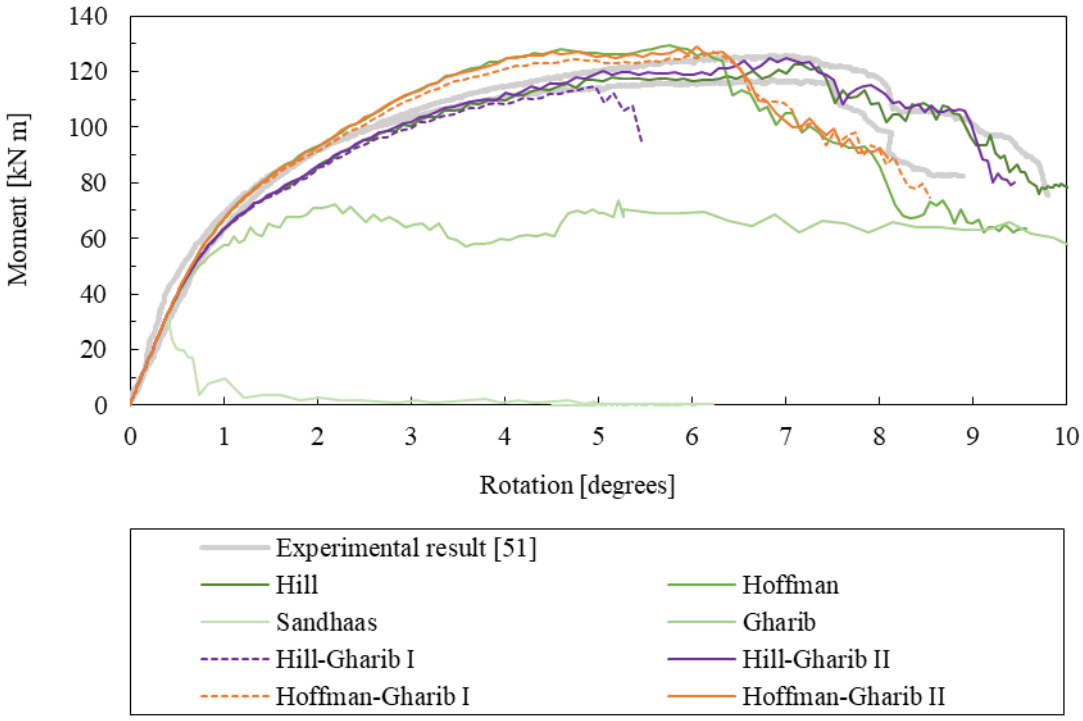

Figure 11. Moment vs rotation plots of FE models with different failure criteria for LVL

The composite Hill-Gharib and Hoffmann-Gharib models perform similarly to Hill and Hoffmann respectively, although Hill-Gharib Case I predicts a somewhat premature failure. No brittle fracture of the timber is reported in [51] for the moment tests, meaning that the similarity between the performance of the Hill and Hoffman and Hill-Gharib and Hoffman-Gharib models is unsurprising.

3.7.2 Shear Simulation

Fig. 12 compares the modelled force-displacement responses with the experimental shear test results in [51]. In all cases, the initial stiffness of the connection is significantly underestimated. This may

be at least partly attributable to an incidental pre-stressing effect imposed during tightening of the bolts, leading to higher than modelled frictional resistance to deformation.

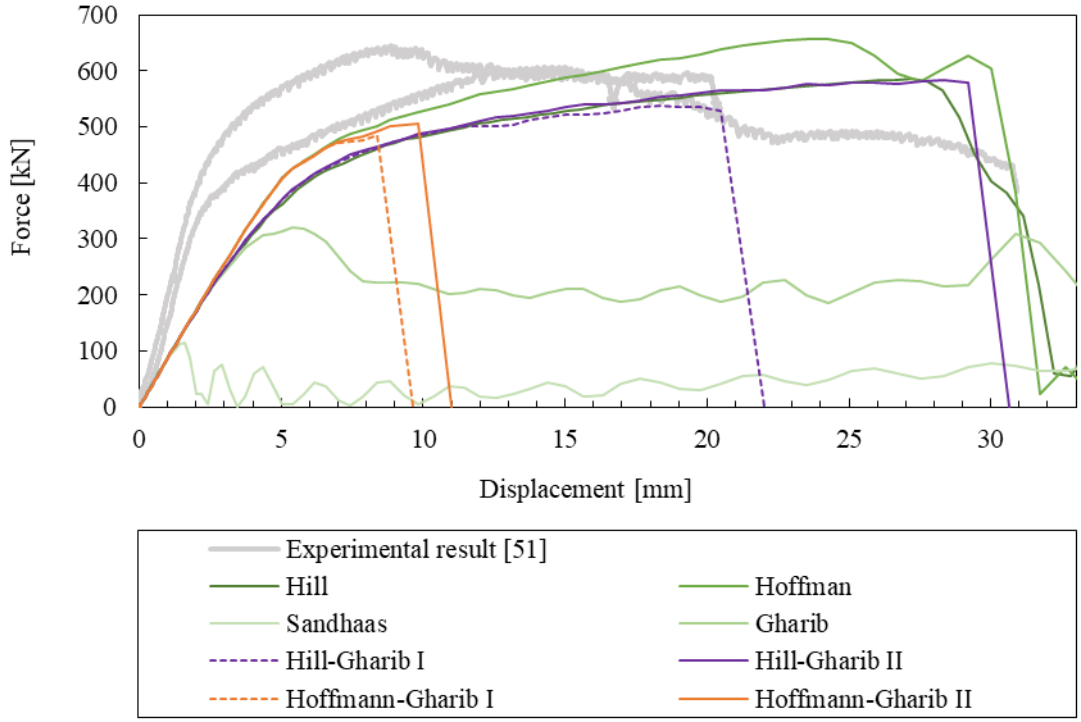

Figure 12: Shear force vs displacement plots of FE models with different failure criteria for LVL

The force-displacement curve from the numerical model with the Hill criterion underestimates the experimental average peak shear force by 4% and overestimates the average displacement at the onset of complete loss of strength by 14%. The Hoffman criterion shows better agreement with the shape of the experimental force-displacement curve with the experimental behaviour but overestimates the experimental average peak shear force by approximately 10%. Neither Hill nor Hoffman criteria capture the perpendicular-to-grain brittle failure in the timber beam observed in [51]. The Sandhaas and Gharib models do not capture the experimental shear force-displacement responses and, as a result of early fracture and rapid damage propagation, significantly underestimate the peak forces and displacements. However, perpendicular-to-grain failure of the timber beam observed in [51] is captured well by these models.

Both cases of the Hill-Gharib models follow a similar force-displacement profile to Hill but Case I predicts failure at a somewhat lesser displacement, agreeing well with one of the two experimental results. Perpendicular-to-grain fracture observed in experiments is also well captured. The discrepancies observed in these FE results, including underestimation of initial stiffness and an overestimation of displacement at the peak shear force, may be attributable to assumed rather than measured material properties for ρ, ε_E^n, G, and friction coefficient taken from the wider literature. The Hoffman-Gharib model does not capture well the experimental force-displacement response, with the experimental average peak shear force under-predicted by approximately 17% and the displacement at the onset of complete loss of strength under-predicted by 68%.

3.7.3 Implications for selection of timber constitutive model

The benchmarked numerical example indicates that Sandhaas and Gharib models are unable to simulate complex timber connection behaviours when used alone. The models using the Hill and Hoffman criteria on the other hand provide reasonably accurate results for the overall moment-rotation of the connection considered, but these are unable to capture the brittle tensile fracture of timber observed in the shear tests. While these examples reaffirm the value of the Hill and Hoffman criteria, they also suggest that complex connection arrangements that may be sensitive to tensile fracture will not be well modelled using these criteria alone. The proposed Hill-Gharib and Hoffman-Gharib models are shown to be capable of capturing both ductile yielding and brittle fracture behaviour of timber in a complex multi-material connection arrangement. In this example, the Hill-Gharib Case-II method best models the experimentally observed behaviours reported in [51].

3.8 Characteristic Element Length

An equivalent plastic deformation, u_{eq}^p, dependent on L, ε_{eq}^{pn} and ε_{eq}^p, for simulating ductile damage of metals was defined in Eq. **(7)**. Although ε_{eq}^{pn} and ε_{eq}^p are material properties and independent of element shape, L depends on the element geometry and formulation. If a part includes different shapes and dimensions, the resulting mesh can be non-uniform, thus having different L values. When

518 the L of an element differs from the L value used to calculate u_{eq}^{p}, the numerical solution adjusts
519 ε_{eq}^{p} of that element to maintain the specified u_{eq}^{p}. Consequently, the failure response of the model
520 may change. In this example, the aluminium connector mesh is highly non-uniform because of
521 different thicknesses and holes having minimum, average and maximum element lengths of 1.70,
522 2.58 and 3.00 mm respectively. The connection was thus modelled for L equal to 1.70, 2.58, and 3.00
523 mm for the estimation of u_{eq}^{p} employing the Hill-Gharib case II and compared with the experimental
524 results in [51] as shown in Fig. 13. The results indicate that modelled behaviour is sensitive to L at
525 larger rotations and displacements. The modelled failure mode was also seen to vary with L,
526 indicating that a study on L is generally necessary to ensure that the full range of possible failure
527 modes and the extent of mesh sensitivity are identified in the case of a non-uniform mesh. While it is
528 preferable to provide a uniform mesh where possible, where this is not possible, L equal to the
529 average element size may provide a reasonable compromise and this was the value adopted in
530 obtaining the results presented in previous sections.

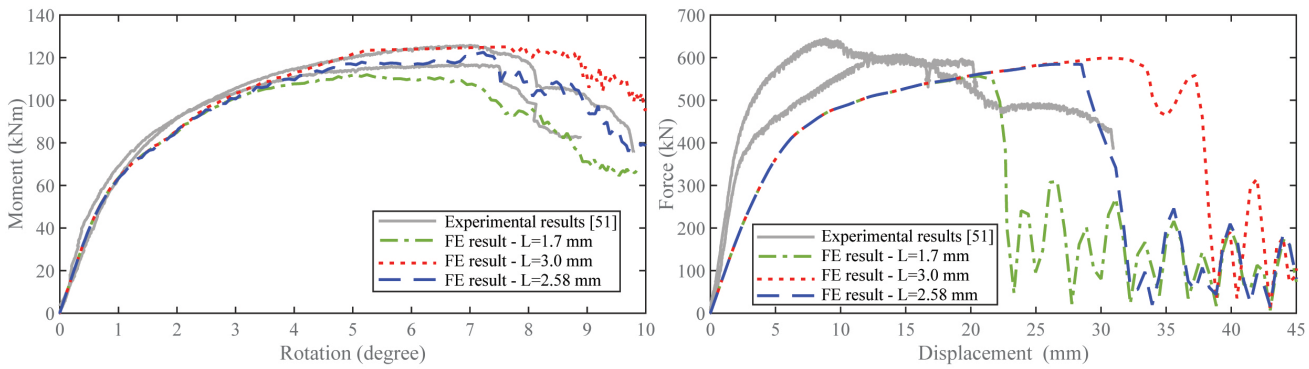

531 (a) (b)

532 **Figure 13: (a) Moment-rotation response and (b) Shear force–displacement response using Hill-Gharib II model.**

533 ## 4 Conclusions

534 Constitutive models and numerical modelling for timber-metal connections through large
535 deformations are presented. A suitable constitutive model for ductile metal components though large
536 deformations including consideration of stress localisation and triaxiality post-necking is described.
537 Some existing constitutive models for timber are discussed, and new constitutive models capturing

both ductile and brittle failure modes are presented. A new formulation of the Hoffmann yield criterion with isotropic hardening for explicit solution is presented, and new VUMAT user subroutines for explicit solution in ABAQUS/Explicit for Hoffmann, Sandhaas, Gharib, Hill-Gharib and Hoffmann-Gharib models are developed and made available for the benefit of other researchers. A benchmarked numerical model is presented for a complex timber, aluminium and steel dowelled beam-column connection tested under shear and moment dominated testing. The numerical results using each of the failure criteria for timber are compared with experimental results [51] and the modelling implications are discussed. The following conclusions are drawn.

- The existing Hoffman criterion, Sandhaas and Gharib models, and the proposed composite Hill-Gharib and Hoffman-Gharib models for timber, can be implemented for explicit solution in the finite element domain using user subroutines developed in this study.
- Numerical modelling using explicit integration methods can capture pre- and post-failure responses of complex timber-metal connections through large deformations. The approach is inherently suited to the simulation of dynamic testing, but it is shown that load-rate modification and mass scaling techniques (Section 3.6) can be applied to allow economical simulation of quasi-static test conditions.
- For complex connection geometries, a parametric study on the characteristic element length L is needed to ensure the reliability of the results without mesh dependency. However, the use of an average element length for L was found to produce acceptable results in the benchmarked numerical example considered.
- Hill-Gharib and Hoffmann-Gharib provide better prediction of failure modes than Hill or Hoffmann alone. While Hill-Gharib and Hoffman-Gharib provide similar moment rotation and load deflection profiles to Hill or Hoffman alone for the benchmarked examples considered, it is anticipated that connection arrangements having a greater dependency on tensile failure of timber will benefit significantly from the use of composite criteria. For the

benchmarked numerical model presented in this study, the proposed Hill-Gharib Case-II criterion produced the most realistic estimations.

5 Acknowledgements

The first author would like to acknowledge Cambridge Commonwealth European and International Trust for the financial support of the Jafar Cambridge Studentship. The numerical modelling was performed using resources provided by the Cambridge Service for Data Driven Discovery using Tier-2 funding from EPSRC capital grant EP/T022159/1 and DiRAC funding from the Science and Technology Facilities Council. The authors would like to express gratitude to Dr. Carmen Sandhaas and Prof. Hamid Valipour for kindly sharing the UMAT codes referred to in this study; and to thank Prof. Benoit Gilbert and team at Griffith University, Australia for generously sharing the experimental data used in this study.

6 Data availability

The VUMAT code for the user subroutines developed in this study are available from the corresponding author upon reasonable request.

7 References

[1] H. Valipour, N. Khorsandnia, K. Crews, and S. Foster, “A simple strategy for constitutive modelling of timber,” *Constr Build Mater*, vol. 53, pp. 138–148, Feb. 2014, doi: 10.1016/J.CONBUILDMAT.2013.11.100.

[2] J. A. J. Huber, M. Ekevad, U. A. Girhammar, and S. Berg, “Structural robustness and timber buildings – a review,” *Wood Mater Sci Eng*, vol. 14, no. 2, pp. 107–128, Mar. 2019, doi: 10.1080/17480272.2018.1446052.

[3] A. M. P. G. Dias, J. W. Van de Kuilen, S. Lopes, and H. Cruz, “A non-linear 3D FEM model to simulate timber–concrete joints,” *Advances in Engineering Software*, vol. 38, no. 8–9, pp. 522–530, Aug. 2007, doi: 10.1016/J.ADVENGSOFT.2006.08.024.

[4] M. Oudjene and M. Khelifa, “Elasto-plastic constitutive law for wood behaviour under compressive loadings,” *Constr Build Mater*, vol. 23, no. 11, pp. 3359–3366, Nov. 2009, doi: 10.1016/J.CONBUILDMAT.2009.06.034.

[5] Jozef GOCÁL, “LOAD CARRYING CAPACITY OF METAL DOWEL TYPE CONNECTIONS OF TIMBER STRUCTURES,” *Civil and Environmental Engineering* , vol. 10, no. 2, pp. 51–60, 2014.

[6] E. Resch and M. Kaliske, “Numerical analysis and design of double-shear dowel-type connections of wood,” *Eng Struct*, vol. 41, pp. 234–241, Aug. 2012, doi: 10.1016/J.ENGSTRUCT.2012.03.047.

[7] Ehsan Jalilifar, Maria Koliou, and Weichiang Pang, “Experimental and Numerical Characterization of Monotonic and Cyclic Performance of Cross-Laminated Timber Dowel-Type Connections,” *Journal of Structural Engineering*, vol. 147, no. 7, 2021.

[8] M. Wang, X. Song, X. Gu, and J. Tang, “Bolted glulam beam-column connections under different combinations of shear and bending,” *Eng Struct*, vol. 181, pp. 281–292, Feb. 2019, doi: 10.1016/J.ENGSTRUCT.2018.12.024.

[9] K. Kildashti, F. Alinoori, F. Moshiri, and B. Samali, “Computational simulation of light timber framing connections strengthened with self-tapping screws,” *Journal of Building Engineering*, vol. 44, p. 103003, Dec. 2021, doi: 10.1016/J.JOBE.2021.103003.

[10] G. D’Arenzo, G. Rinaldin, M. Fossetti, and M. Fragiacomo, “An innovative shear-tension angle bracket for Cross-Laminated Timber structures: Experimental tests and numerical

607 modelling," *Eng Struct*, vol. 197, p. 109434, Oct. 2019, doi:
608 10.1016/J.ENGSTRUCT.2019.109434.

609 [11] H. Yang, W. Liu, and X. Ren, "A component method for moment-resistant glulam beam–
610 column connections with glued-in steel rods," *Eng Struct*, vol. 115, pp. 42–54, May 2016, doi:
611 10.1016/J.ENGSTRUCT.2016.02.024.

612 [12] X. Cheng, B. P. Gilbert, H. Guan, D. Dias-da-Costa, and H. Karampour, "Influence of the
613 earthquake and progressive collapse strain rate on the structural response of timber dowel type
614 connections through finite element modelling," *Journal of Building Engineering*, vol. 57, p.
615 104953, Oct. 2022, doi: 10.1016/J.JOBE.2022.104953.

616 [13] T. Gečys, A. Daniunas, T. K. Bader, L. Wagner, and J. Eberhardsteiner, "3D finite element
617 analysis and experimental investigations of a new type of timber beam-to-beam connection,"
618 *Eng Struct*, vol. 86, pp. 134–145, Mar. 2015, doi: 10.1016/J.ENGSTRUCT.2014.12.037.

619 [14] D. Oliveira, C. Viau, and G. Doudak, "Modelling the behaviour of heavy and mass timber
620 members subjected to blast loads," *Eng Struct*, vol. 291, p. 116397, Sep. 2023, doi:
621 10.1016/J.ENGSTRUCT.2023.116397.

622 [15] X. Sun, Y. Qu, W. Liu, W. Lu, and S. Yuan, "Rotational behavior and modeling of bolted
623 glulam beam-to-column connections with slotted-in steel plate,"
624 *https://doi.org/10.1177/1369433220906223*, vol. 23, no. 9, pp. 1989–2000, Feb. 2020, doi:
625 10.1177/1369433220906223.

626 [16] E. L. Grimsmo, A. Aalberg, M. Langseth, and A. H. Clausen, "Failure modes of bolt and nut
627 assemblies under tensile loading," *J Constr Steel Res*, vol. 126, pp. 15–25, Nov. 2016, doi:
628 10.1016/J.JCSR.2016.06.023.

[17] M. Pavlović, Z. Marković, M. Veljković, and D. Bucrossed D Signevac, "Bolted shear connectors vs. headed studs behaviour in push-out tests," *J Constr Steel Res*, vol. 88, pp. 134–149, Sep. 2013, doi: 10.1016/J.JCSR.2013.05.003.

[18] N. Khorsandnia, H. R. Valipour, and K. Crews, "Nonlinear finite element analysis of timber beams and joints using the layered approach and hypoelastic constitutive law," *Eng Struct*, vol. 46, pp. 606–614, Jan. 2013, doi: 10.1016/J.ENGSTRUCT.2012.08.017.

[19] L. Daudeville, "Fracture in spruce: Experiment and numerical analysis by linear and non linear fracture mechanics," *Holz als Roh - und Werkstoff*, vol. 57, no. 6, pp. 425–432, 1999, doi: 10.1007/S001070050068/METRICS.

[20] R. Hill, "A Theory of the Yielding and Plastic Flow of Anisotropic Metals," *RSPSA*, vol. 193, no. 1033, pp. 281–297, May 1948, doi: 10.1098/RSPA.1948.0045.

[21] O. Hoffman, "The Brittle Strength of Orthotropic Materials," *http://dx.doi.org/10.1177/002199836700100210*, vol. 1, no. 2, pp. 200–206, Apr. 1967, doi: 10.1177/002199836700100210.

[22] S. W. Tsai and E. M. wu, "A General Theory of Strength for Anisotropic Materials," *http://dx.doi.org/10.1177/002199837100500106*, vol. 5, no. 1, pp. 58–80, Jan. 1971, doi: 10.1177/002199837100500106.

[23] Z. Li, Y. Wang, X. Liu, J. Ou, Z. Gan, and M. He, "Mechanical performance of glulam beam-to-column joints with geometrical modulus: Experimental investigation and analytical approach," *Journal of Building Engineering*, vol. 84, p. 108437, May 2024, doi: 10.1016/J.JOBE.2024.108437.

[24] B. H. Xu, M. Taazount, A. Bouchaïr, and P. Racher, "Numerical 3D finite element modelling and experimental tests for dowel-type timber joints," *Constr Build Mater*, vol. 23, no. 9, pp. 3043–3052, Sep. 2009, doi: 10.1016/J.CONBUILDMAT.2009.04.006.

[25] H. Eslami, L. B. Jayasinghe, and D. Waldmann, "Nonlinear three-dimensional anisotropic material model for failure analysis of timber," *Eng Fail Anal*, vol. 130, p. 105764, Dec. 2021, doi: 10.1016/J.ENGFAILANAL.2021.105764.

[26] S. T. Akter, E. Serrano, and T. K. Bader, "Numerical modelling of wood under combined loading of compression perpendicular to the grain and rolling shear," *Eng Struct*, vol. 244, p. 112800, Oct. 2021, doi: 10.1016/J.ENGSTRUCT.2021.112800.

[27] N. T. Mascia and R. A. Simoni, "Analysis of failure criteria applied to wood," *Eng Fail Anal*, vol. 35, pp. 703–712, Dec. 2013, doi: 10.1016/J.ENGFAILANAL.2013.07.001.

[28] L. Zhang, Y. Han, Q. Xie, Y. Wang, and Y. Wu, "Mechanical performance of wood subjected to the interaction of transversal tension/compression and longitudinal shear stresses," *Constr Build Mater*, vol. 420, p. 135637, Mar. 2024, doi: 10.1016/J.CONBUILDMAT.2024.135637.

[29] V. Bucur, S. Garros, and C. Y. Barlow, "The effect of hydrostatic pressure on physical properties and microstructure of spruce and cherry," *Holzforschung*, vol. 54, no. 1, pp. 83–92, Jan. 2000, doi: 10.1515/HF.2000.013/MACHINEREADABLECITATION/RIS.

[30] P. Mackenzie-Helnwein, J. Eberhardsteiner, and H. A. Mang, "A multi-surface plasticity model for clear wood and its application to the finite element analysis of structural details," *Comput Mech*, vol. 31, no. 1-2 SPEC., pp. 204–218, 2003, doi: 10.1007/S00466-003-0423-6/METRICS.

[31] J. Schmidt and M. Kaliske, "Models for numerical failure analysis of wooden structures," *Eng Struct*, vol. 31, no. 2, pp. 571–579, Feb. 2009, doi: 10.1016/J.ENGSTRUCT.2008.11.001.

673 [32] K. Hofstetter, C. Hellmich, and J. Eberhardsteiner, “Development and experimental validation
674 of a continuum micromechanics model for the elasticity of wood,” *European Journal of*
675 *Mechanics - A/Solids*, vol. 24, no. 6, pp. 1030–1053, Nov. 2005, doi:
676 10.1016/J.EUROMECHSOL.2005.05.006.

677 [33] Z. Hashin, “Failure criteria for unidirectional fiber composites,” *Journal of Applied*
678 *Mechanics, Transactions ASME*, vol. 47, no. 2, pp. 329–334, 1980, doi: 10.1115/1.3153664.

679 [34] C. Sandhaas, J.-W. G. van de Kuilen, and H. J. Blass, “A 3D CONSTITUTIVE WOOD
680 MODEL USING THE CONCEPTS OF CONTINUUM DAMAGE MECHANICS,” in
681 *European Congress on Computational Methods in Applied Sciences and Engineering*
682 *(ECCOMAS 2012)*, Vienna, Austria, Sep. 2012.

683 [35] A. Hassanieh, H. R. Valipour, M. A. Bradford, and C. Sandhaas, “Modelling of steel-timber
684 composite connections: Validation of finite element model and parametric study,” *Eng Struct*,
685 vol. 138, pp. 35–49, May 2017, doi: 10.1016/J.ENGSTRUCT.2017.02.016.

686 [36] M. Gharib, A. Hassanieh, H. Valipour, and M. A. Bradford, “Three-dimensional constitutive
687 modelling of arbitrarily orientated timber based on continuum damage mechanics,” *Finite*
688 *Elements in Analysis and Design*, vol. 135, pp. 79–90, Nov. 2017, doi:
689 10.1016/J.FINEL.2017.07.008.

690 [37] A. Hassanieh, H. R. Valipour, and M. A. Bradford, “Bolt shear connectors in grout pockets:
691 Finite element modelling and parametric study,” *Constr Build Mater*, vol. 176, pp. 179–192,
692 Jul. 2018, doi: 10.1016/J.CONBUILDMAT.2018.05.029.

693 [38] M. Khelifa, A. Khennane, M. El Ganaoui, and A. Celzard, “Numerical damage prediction in
694 dowel connections of wooden structures,” *Materials and Structures/Materiaux et*

Constructions, vol. 49, no. 5, pp. 1829–1840, May 2016, doi: 10.1617/S11527-015-0615-5/TABLES/4.

[39] B.-H. Xu, A. Bouchaïr, and P. Racher, "Appropriate Wood Constitutive Law for Simulation of Nonlinear Behavior of Timber Joints," *Journal of Materials in Civil Engineering*, vol. 26, no. 6, p. 04014004, Jun. 2014, doi: 10.1061/(ASCE)MT.1943-5533.0000905/ASSET/DDE4F277-E787-4239-84EB-BE23B27E06E1/ASSETS/IMAGES/LARGE/FIGURE11.JPG.

[40] M. Wang, X. Song, A. M. Asce, and X. Gu, "Three-Dimensional Combined Elastic-Plastic and Damage Model for Nonlinear Analysis of Wood," *Journal of Structural Engineering*, vol. 144, no. 8, Aug. 2018, doi: 10.1061/(ASCE)ST.1943-541X.0002098.

[41] C. A. Schuh and A. C. Lund, "Atomistic basis for the plastic yield criterion of metallic glass," *Nature Materials 2003 2:7*, vol. 2, no. 7, pp. 449–452, Jun. 2003, doi: 10.1038/nmat918.

[42] S. Tu, X. Ren, J. He, and Z. Zhang, "Stress–strain curves of metallic materials and post-necking strain hardening characterization: A review," *Fatigue Fract Eng Mater Struct*, vol. 43, no. 1, pp. 3–19, Jan. 2020, doi: 10.1111/FFE.13134.

[43] M. Gromada, G. Mishuris, and A. Öchsner, *Correction Formulae for the Stress Distribution in Round Tensile Specimens at Neck Presence*. SpringerLink, 2011.

[44] A. Hillerborg, M. Modéer, and P. E. Petersson, "Analysis of crack formation and crack growth in concrete by means of fracture mechanics and finite elements," *Cem Concr Res*, vol. 6, no. 6, pp. 773–781, Nov. 1976, doi: 10.1016/0008-8846(76)90007-7.

[45] Dassault Systèmes Simulia Corp, "Abaqus User's Manual." 2020.

[46] R. M. Foster and M. H. Ramage, "Tall timber," *Nonconventional and Vernacular Construction Materials: Characterisation, Properties and Applications*, pp. 467–490, Jan. 2020, doi: 10.1016/B978-0-08-102704-2.00017-2.

[47] D. R. J. OWEN and E. HINTON, *Finite Elements in Plasticity: Theory and Practice*. Pineridge Press Limited, Swansea, U.K, 1980.

[48] W. Han and B. D. Reddy, *Plasticity: Mathematic Theory and Numerical Analysis*. Springer-Verlag New York, Inc, 1999.

[49] M. Alzweighi, R. Mansour, J. Tryding, and A. Kulachenko, "Evaluation of Hoffman and Xia plasticity models against bi-axial tension experiments of planar fiber network materials," *Int J Solids Struct*, vol. 238, p. 111358, 2022, doi: 10.1016/j.ijsolstr.2021.111358.

[50] A. Karimi-Nobandegani, M. Gharib, and H. Valipour, "A nonlocal continuum damage model for timber: Development, implementation, and application," *Eng Fract Mech*, vol. 277, p. 109009, Jan. 2023, doi: 10.1016/J.ENGFRACMECH.2022.109009.

[51] M. Masaeli, B. P. Gilbert, H. Karampour, I. D. Underhill, C. H. Lyu, and S. Gunalan, "Scaling effect on the moment and shear responses of three types of beam-to-column connectors used in mass timber buildings," *Eng Struct*, vol. 208, p. 110329, Apr. 2020, doi: 10.1016/J.ENGSTRUCT.2020.110329.

[52] M. Dorn, K. de Borst, and J. Eberhardsteiner, "Experiments on dowel-type timber connections," *Eng Struct*, vol. 47, pp. 67–80, Feb. 2013, doi: 10.1016/J.ENGSTRUCT.2012.09.010.

[53] M. Stehr and I. Johansson, "Weak boundary layers on wood surfaces," *J Adhes Sci Technol*, vol. 14, no. 10, pp. 1211–1224, Jan. 2000, doi: 10.1163/156856100742168.

[54] L. M. M. B. Jayasekara and R. M. Foster, "NUMERICAL MODELLING OF MASS TIMBER BEAM-COLUMN CONNECTIONS," *13th World Conference on Timber Engineering, WCTE 2023*, vol. 5, pp. 2841–2850, 2023, doi: 10.52202/069179-0372.

[55] R. J. M. Pijpers and H. M. Slot, “Friction coefficients for steel to steel contact surfaces in air and seawater,” *J Phys Conf Ser*, vol. 1669, no. 1, p. 012002, Oct. 2020, doi: 10.1088/1742-6596/1669/1/012002.

[56] M. Dorn, K. Habrová, R. Koubek, and E. Serrano, “Determination of coefficients of friction for laminated veneer lumber on steel under high pressure loads,” *Friction*, vol. 9, no. 2, pp. 367–379, Apr. 2021, doi: 10.1007/S40544-020-0377-0/METRICS.

[57] J. R. Air, F. Arriaga, G. Iniguez-Gonzalez, and J. Crespo, “Static and kinetic friction coefficients of scots pine (pinus sylvestris l.), parallel and perpendicular to grain direction,” *Materiales de Construccion*, vol. 64, no. 315, Jul. 2014, doi: 10.3989/MC.2014.03913.

[58] M. Basterrechea-Arévalo, J. M. Cabrero, B. Iraola, and R. Goñi, “Modelling of moment transmitting beam-to-column timber connections accounting for frictional transmission,” *Eng Struct*, vol. 247, p. 113122, Nov. 2021, doi: 10.1016/J.ENGSTRUCT.2021.113122.

[59] M. Dorn, “Investigations on the serviceability limit state of dowel-type timber connections,” E202 - Institut für Mechanik der Werkstoffe und Strukturen , 2012.

[60] J. Ribeiro, A. Santiago, and C. Rigueiro, “Damage model calibration and application for S355 steel,” *Procedia Structural Integrity*, vol. 2, pp. 656–663, Jan. 2016, doi: 10.1016/J.PROSTR.2016.06.085.

[61] K. Frühmann, E. K. Tschegg, C. Dai, and S. E. Stanzl-Tschegg, “Fracture behaviour of laminated veneer lumber under mode I and III loading,” *Wood Sci Technol*, vol. 36, no. 4, pp. 319–334, Aug. 2002, doi: 10.1007/S00226-002-0142-8/METRICS.

[62] X. Cheng, ; Benoit, P. Gilbert, C. Lyu, and H. Guan, “Strain Rate Effect on the Embedment Mechanical Properties and Fracture Behavior of Softwood Laminated Veneer Lumbers:

Implications to Timber Connections," *Journal of Structural Engineering*, vol. 149, no. 9, Sep. 2023, doi: 10.1061/JSENDH.STENG-12508.